Ti-6Al-4V powder characteristics in laser powder bed fusion: The effect on tensile and fatigue behavior

Arash Soltani-Tehrani [a,b], Mahdi Habibnejad-Korayem [c], Shuai Shao [a,b], Meysam Haghshenas [d], Nima Shamsaei [a,b,*]

[a] *National Center for Additive Manufacturing Excellence (NCAME), Auburn University, Auburn, AL 36849, USA*
[b] *Department of Mechanical Engineering, Auburn University, Auburn, AL 36849, USA*
[c] *External R&D, AP&C, a GE Additive Company, St-Eustache, QC J7R 0L5, Canada*
[d] *Department of Mechanical, Industrial and Manufacturing Engineering, The University of Toledo, Toledo, OH 43606, USA*

ARTICLE INFO

ABSTRACT

This work investigates the effects of powder characteristics, particularly particle size distribution (PSD), on the micro-/defect-structure, tensile, and fatigue properties of Grade 23 Ti-6Al-4V specimens as well as how these effects are influenced by the build location and specimens' surface finish. Two batches of plasma atomized Ti-6Al-4V powder feedstock with two different PSDs of 15–45 μm (fine) and 15–53 μm (coarse) were used for fabrication. Both batches exhibited excellent rheological properties with moderate improvement noted in the fine batch. The influence of PSDs was shown to be small on the resulting microstructure and surface roughness of the specimens, while significant on the volumetric defect distribution. In addition, machined specimens fabricated from coarse powder exhibited somewhat enhanced ductility, smaller defects, and some improvements in the fatigue properties as compared to the fine powder specimens. These variations were correlated with lower tendency of spattering in coarse powder. Process-induced silicon-rich spatters, which were detrimental to both tensile and fatigue properties, were more prevalent in the specimens built from the fine powder batch, and were ascribed to the rapid decomposition of SiO_2. Owing to the highly spherical particles and the resulting excellent flowability of both batches, defect content and mechanical properties did not show strong location dependency.

1. Introduction

Additive manufacturing (AM) has gained significant attention from industrial sectors and governmental agencies, by providing manufacturers with more design freedom and the ability to fabricate complex geometries and reduce material waste. This booming interest to generate functional parts for load-bearing applications has also introduced some challenges toward mass production with AM technologies, which necessitates a more thorough understanding of the feedstock-part performance relationships [1,2]. One of the most critical facets is the state of the material feedstock − whether in the form of wire or powder, feedstock characteristics (i.e., morphology, chemistry, and microstructure [3]) can affect the mechanical performance of additively manufactured (AM) parts. In the case of laser or electron powder bed fusion (L-PBF or E-PBF) AM, where the powder is used as the feedstock, the particle size and morphology can play a critical role on the mechanical performance of the fabricated parts.

Morphological characteristics can be mainly divided into particle shape and size distribution, which have been reported to influence the surface roughness, volumetric defect content, and mechanical behavior—as well as their location dependency—of AM parts [4,5]. It has been well established that using a powder batch with highly spherical particles can improve powder flowability, spreadability, and packing state as a result of less interparticle friction [4]. However, when it comes to particle size and particle size distribution (PSD), choosing the appropriate range can be challenging. On one hand, the presence of fine particles in coarse ones can theoretically lead to a more densely packed powder bed. On the other hand, excess amount of fine particles—due to the higher surface area and more interparticle friction—can result in

---

Nomenclature

$2N_f$	number of reversals to failure
ε_f	true fracture strain
R_σ	ratio of minimum to maximum stress
R_a	arithmetical mean height of the profiled line
σ_a	stress amplitude
Coarse/Fine powders	The PSD of coarse and fine powder batches were 15–53 μm and 15–45 μm, respectively
East/West specimens	East specimens were closer to the powder feedstock while the West ones were further away
Gas-entrapped pore	An AM process-induced volumetric defect formed due to entrapment of shielding gas
Lack-of-fusion defect	An AM process-induced volumetric defect formed due to insufficient overlap between molten tracks or between layers
Void	A tensile loading induced cavity within the material which can grow and coalesce with the neighboring voids to induce fracture

increased oxygen pickup as well as particle interlocking (i.e., agglomeration) which can reduce powder's overall flowability and spreadability and lead to poor powder bed packing [6,7].

The differences in the powder bed packing state may influence the tensile, fatigue, and fracture properties since they can generate different surface roughness, volumetric defect contents, and microstructure in the fabricated parts. In terms of surface roughness, although it is generally acknowledged that the as-built rough surface compromises the tensile ductility and fatigue properties of AM specimens compared to machined and polished surfaces, how the surface roughness is affected by powder characteristics and rheological properties is not clear. While coarser particle size has been shown to lead to higher values in certain roughness parameters [3,4], such as the R_a (arithmetical mean deviation of a surface line profile), how well these popular parameters correlate with the mechanical properties, especially fatigue, is still debated. Therefore, it can be stated that the effect of powder characteristics on the mechanical properties of AM specimens with as-built surfaces is not well understood (***Knowledge Gap #1***).

In terms of volumetric defect content, coarser/larger particles that are relatively uniform in size have better flowability and are typically associated with lower defect contents in parts, even though the theoretical powder bed packing density is relatively low [8]. On the other hand, the hindered powder flow due to a large number of fine particles can give rise to inconsistent deposition of powder, empty pockets due to agglomerates, and higher defect content with strong location dependency [5]. The volumetric defects (e.g., gas-entrapped pores) generally do not affect the yield strength (YS) of materials, but they may be detrimental to their ductility and the ultimate tensile strength (UTS) since they are effective nucleation sites for tension-induced voids [9].

For instance, Jian et al. [10] observed lower defect content in parts fabricated by a coarser AlSi10Mg powder batch in L-PBF, which yielded a much higher ductility (almost twice) and a moderately increased UTS, but essentially the same YS compared with finer powder-produced ones. This observation was echoed by the results provided by Riener et al. [11] for L-PBF AlSi10Mg. Similarly, Brika et al. [6] have shown that specimens manufactured from a coarser Ti-6Al-4 V (Ti64) powder batch via L-PBF had a higher part density (lower defect content), true fracture strain (ε_f), and UTS as compared to their counterparts fabricated from the finer powder batch [6]. However, although existing studies have investigated the effect of fine and coarse particles, the effect of wider/narrower PSD span has not been addressed (***Knowledge Gap #2***).

In terms of microstructure, the inter-particle contact may be inefficient in a poorly packed powder bed which may be associated with slightly lower thermal conductivity [12], slightly lower cooling rate, coarser microstructure, and thus slightly lower YS. This is supported by the E-PBF data reported by Nandwana et al. [13], where a coarser α-lath thickness was noticed in the typical α + β basketweave microstructure in the finer powder specimens. A lower UTS by about 6% for the specimens fabricated from the fine Ti64 powder batch was also reported. Although YS was not reported in this study, the same trend should hold since the strain hardening rate of Ti64 is very low [2,14].

While tensile properties of AM parts are affected by powder characteristics via both defect content and microstructure, the fatigue properties are primarily dictated by both surface and volumetric defects [15,16], more so in the high cycle fatigue (HCF) regime. In the machined surface condition, the effect of volumetric defect becomes apparent. For instance, Soltani-Tehrani et al. [5] reported that reusing the 17–4 PH stainless steel (SS) powder in an L-PBF system can result in smaller defects by changing the PSD, and consequently an enhanced HCF performance. Similar influence of PSD and powder rheological properties on defect characteristics and fatigue performance in the resulting materials were echoed by other studies such as Ref. [10,13]. However, the correlation of fatigue properties with powder characteristics, including their rheological properties, is still lacking (***Knowledge Gap #3***). Interestingly, the validity of the "coarser powder-better properties" trend noted above is not always true. For instance, Jian et al. [10] witnessed a higher fatigue resistance for the L-PBF AlSi10Mg specimens fabricated from the coarser batch (average particle size of 50 μm), while Nandwana et al. [13] reported that being inferior for the coarser Ti64 batch (median size of 90 μm, 10th percentile size of 71.4 μm) in E-PBF AM. It is expected that excessively large particles are inefficient to absorb the incident energy which could lead to poor melting and defect formation [11,17].

Lastly, in the PBF technologies, the powder is distributed from the reservoir on one side of the powder bed to the other; thus, the packing state of powder may be location-dependent [5,18]. This location dependency has been primarily associated with powder flowability and spreadability [5]. To uncover such a correlation between the powder and location, Jacob et al. [18] investigated the spreadability of Inconel 718 and 17–4 PH SS with different PSDs. It was observed that the segregation of powder particles (i.e., the separation of the powder size constituents [19]) can result in the non-uniform deposition of powder in different locations. This behavior was explained by the "front stress-free turning powder wedge" phenomenon, which states that finer particles typically move to the bottom of the powder bulk, and consequently, are deposited closer to the dispenser, while coarser ones might deposit near the overflow bin (i.e., collector) [18,20]. The location-dependent powder bed packing state may produce defect content and mechanical properties of the resulting parts that are also location-specific [5]. However, this location dependency has hitherto been underexplored (***Knowledge Gap #4***).

To address the four knowledge gaps defined, this work evaluates the effect of powder characteristics on powder rheological behavior as well as on the microstructure, surface roughness volumetric defect content, and mechanical properties—and their location dependency—of L-PBF Ti64 parts. Ti64 is the most widely used titanium alloy in PBF technologies due to its high strength, low weight, biocompatibility, and corrosion resistance which has made it a suitable raw material for aviation, space, biomedical, and chemical applications [21]. Two batches of Ti64 powder with different PSD ranges (i.e., 15–53 μm and 15–45 μm) were utilized for fabrication, whose morphological and rheological characteristics were thoroughly characterized and used to correlate with the variations observed in tensile and fatigue properties of the fabricated parts. To investigate the location dependency of microstructural, defect, and mechanical properties, parts were placed across different locations on the build plate in the powder distribution direction and tracked during fabrication. This article is arranged as the following: Section 2 Methodology, Section 3 Experimental Results, and Section 4 Discussion on Experimental Results. Finally, conclusions are

drawn in Section 5 based on the results and discussion.

2. Methodology

In this study, two powder batches of Advanced Powders and Coating (AP&C) plasma atomized spherical Ti64 Grade 23 with two different PSDs of 15–53 μm and 15–45 μm were used for fabrication. Hereon, the two powder batches are referred to respectively as "coarse" and "fine" throughout the manuscript. The chemical composition following the ASTM F3001 [22] and measured based on ASTM E1409, E1447, E1941, and E2371 [23–26], as well as D_{10}, D_{50}, D_{90} sizes obtained by laser diffraction according to ASTM B822 [27] for both batches are reported in Table 1. The D_x value signifies the xth percentile particle size, i.e., x% of the particles are smaller than D_x μm [4]. The span value is defined as the $(D_{90}-D_{10})/D_{50}$ [6]. Both batches were sieved using an 80-μm filter before loading the feedstock bin to ensure there are no exceedingly large particles or agglomerates in the batch. The same layout (shown in Fig. 1 (a) and Fig. 1(b)) was designed and used for fabrication from both powder batches via EOS M290, an L-PBF AM machine, using the process parameters listed in Table 2. In this table, the energy density level associated with the infill parameters was also calculated which was the ratio of laser power to hatching distance, scanning speed, and layer thickness [28].

In the build layout, 32 net-shaped fatigue specimens (geometry according to ASTM E466 [29]) to be tested in the as-built surface condition were included (see Fig. 1(c)). In addition, 60 cylindrical rods were fabricated, among which, 24 rods were machined to the geometries of fatigue specimens (20 rods) according to ASTM E466 [29] (see Fig. 1(d)) and tension specimens (4 rods) according to ASTM E8M [30] (see Fig. 2 (e)) and were tested in the machined surface condition. Two tensile tests were performed for per powder batch per location. The build layout also contained some half-built cylindrical bars (referred to hereafter as microstructural samples) which were used to characterize the microstructure representative of the build height at the gage of the test specimens. The specimens were specifically placed in two locations, including the East, i.e., closer to the feedstock bin, and the West, i.e., farther away from the feedstock bin to investigate the effects of location on the mechanical properties as well.

After fabrication, parts were detached from the build plate then annealed at 900 °C for 1 h and furnace-cooled in an argon environment. This heat treatment of L-PBF Ti64 has been reported to decompose its martensitic microstructure and result in lamellar $\alpha + \beta$ and slightly higher fatigue strength as compared to stress relief at 740 °C for about two hours [31]. Before the test, the machined specimens were polished using sandpapers with reducing grit. Tensile tests were performed in displacement-controlled mode with a nominal strain rate of

0.001 mm/mm/s according to ASTM E8M [30] via MTS Landmark servohydraulic axial test system equipped with a 100-kN load cell. An extensometer was attached to the specimen initially and was removed at 0.05 mm/mm strain to protect the extensometer from any damage. The tensile tests were continued until fracture in displacement-controlled mode. After the fracture, true fracture strain ε_f, 0.2% offset YS, and UTS were measured and calculated. The fracture surfaces of some tensile test specimens were examined using the Zeiss Crossbeam 550 scanning electron microscope (SEM).

In addition, fully-reversed fatigue tests ($R_\sigma = -1$) were conducted in the force-controlled mode for both as-built and machined specimens based on ASTM E466 [29] using an MTS Bionix Tabletop axial test system supplied with a 25-kN load cell. Different stress levels were applied on specimens to acquire properties in high- and mid- cycle fatigue (HCF and MCF) regimes. Test frequency was chosen at each stress level to ensure a constant average cyclic strain rate for all specimens. Each test was continued until the complete separation of the specimen. After failure, both pieces of the fractured specimen were protected for further fracture surface analysis. All tests that endured 5×10^6 cycles (i. e., 10^7 reversals) were stopped and considered as run-out (no failure) tests. Fracture surfaces of fatigue specimens were later investigated via a Keyence VHX-6000 digital optical microscope. Using microscopy, the crack initiation sites were identified and the defect size was measured with the built-in software.

The R_a surface roughness, i.e., the arithmetical mean height of profiled lines, was evaluated in all East and West as-built specimens fabricated from either coarse or fine powder batches using the Keyence microscope. The measurements were performed in a 3-mm length in the gauge section from five different locations to verify the results. To capture the defect content, 2 machined fatigue specimens per powder type in each location (a total of 8 specimens) were selected and scanned via Zeiss Xradia 620 Versa at 140 kV voltage and 21 W power. The source and detector were positioned in a way to reach a voxel size of 6 μm. Finally, the Zeiss built-in software was used to reconstruct the images. Reconstructed images were then processed with ImageJ to assess the defect distributions. In addition, 3D visualizations were generated via Dragonfly software.

Microstructural samples were cut parallel to the building direction, mounted in the longitudinal plane, and were polished to achieve a mirror-like surface finish. After polishing, electron backscatter diffraction (EBSD) scans were performed via the Zeiss Crossbeam 550 SEM to obtain the microstructure. The Freeman Technology FT4 powder rheometer was also used to characterize the rheological properties of powder batches, which were sampled following ASTM B215 [32] before and after the sieving process from the feedstock bin. Powder characteristics including compressibility, permeability, cohesion, conditioned bulk and tapped densities (ASTM B527 [33]), and shear stress (ASTM D7891 [34]) were quantified via FT4. Particle morphology and surface chemistry were also evaluated by the SEM and energy-dispersive X-ray spectroscopy (EDS). Lastly, the PSDs were assessed via a Beckman Coulter LS 13 320 laser diffraction particle size analyzer according to ASTM B822 [27].

3. Experimental results

3.1. Powder characteristics

The morphology of both powder batches in the unused (i.e., virgin) condition was assessed via the SEM and shown in Fig. 2(a)-(b). It appears that both coarse and fine batches consist of highly spherical particles that are relatively uniform in size, despite a few irregularly-shaped ones that may form due to the atomization process or powder handling. These features are consistent with the output of plasma atomization, which typically produces very spherical particles, narrow PSDs, and fewer internal defects (i.e., gas-entrapped pores in powder particles) [3,4,35]. In the magnified views in Fig. 2(a)-(b), some fine particles as well as

Table 1

Chemical composition and D_{10}, D_{50}, and D_{90} parameters of the coarse and fine Ti64 powder batches.

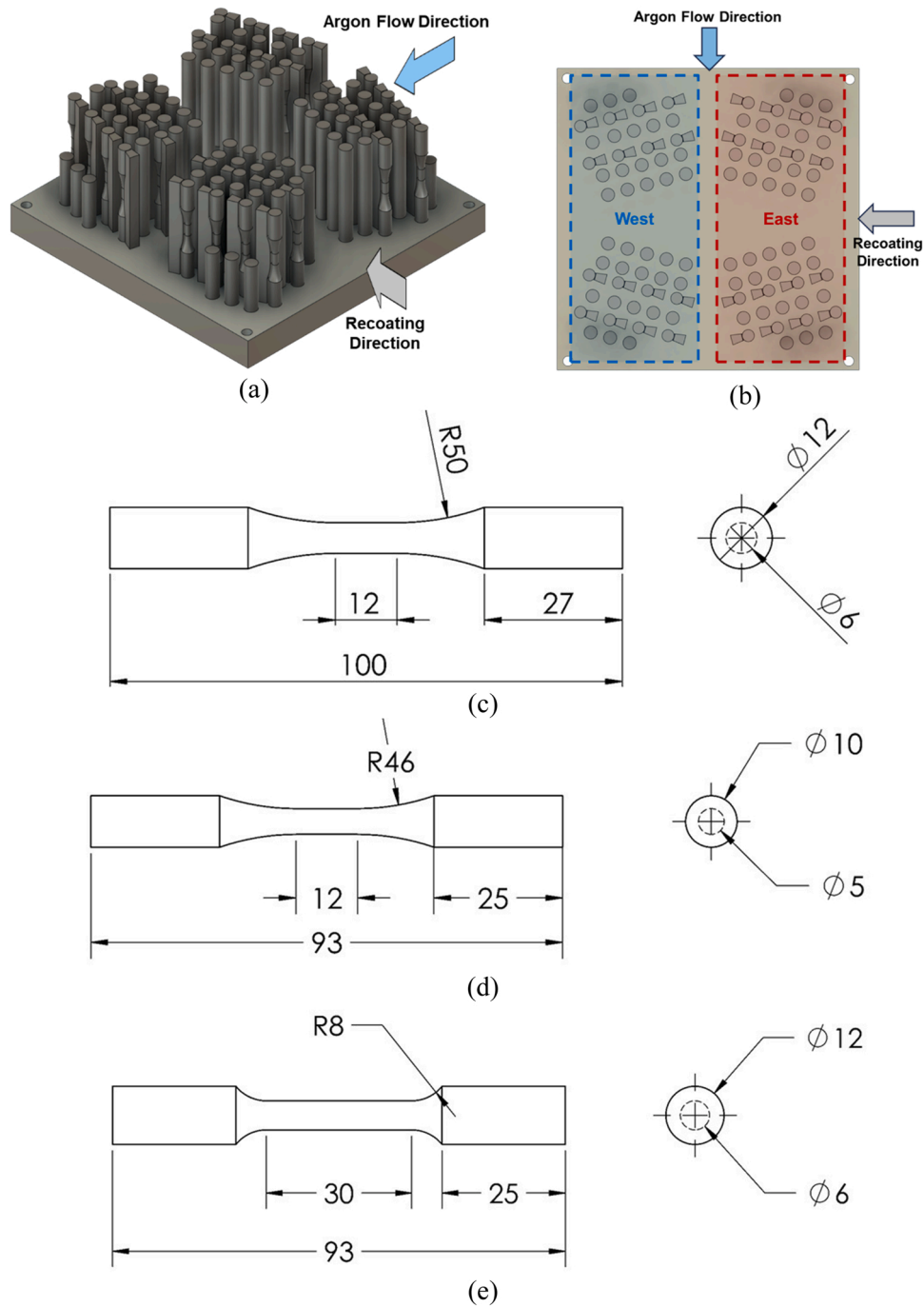| Powder	Coarse Ti64	Fine Ti64	Testing Method
Element (wt%)			
Al	6.394	6.409	ASTM E2371
V	3.920	3.933	
Fe	0.204	0.202	
Y	< 0.001	< 0.001	
O	0.096	0.118	ASTM E1409
N	0.015	0.014	
H	0.002	0.002	ASTM E1447
Others Each	< 0.080	< 0.080	ASTM E2371
Others Total	< 0.200	< 0.200	
Ti	Balance	Balance	–
Particle Size Distribution (PSD)			
D_{10}	23 μm	20 μm	ASTM B822
D_{50}	45 μm	34 μm	
D_{90}	57 μm	44 μm	
Span	0.76	0.71	

Fig. 1. Fabrication layout in (a) isometric and (b) top views. The layout consisted of (c) as-built fatigue specimens according to ASTM E466 with a gage diameter of 6 mm [29] and cylindrical bars which were machined to (d) fatigue specimens with a gage diameter of 5 mm according to ASTM E466 [29] and (e) round tension test specimens according to ASTM E8M [30].

Table 2
EOS M290 Infill and contour process parameters for Ti64 along with the calculated energy densities.

Parameter Set	Laser Power P (W)	Scanning Speed V (mm/s)	Hatching Distance H (mm)	Layer Thickness t (µm)	Energy Density E (J/mm³)
Infill	280	1200	0.14	30	55.6
Contour	150	1250	–	30	–

satellites, are present in both batches. It needs to be emphasized that 2D morphological analysis may not completely represent the 3D features of powder particles. Ideally, 3D morphological analysis using X-ray CT is

recommended [36–39] to obtain particle geometries accurately.

As seen in Fig. 2(c), the surface chemistry in terms of the major alloying elements (i.e., Ti, Al, and V), obtained from EDS and performed on the shaded particles in Fig. 2(a)-(b) revealed no significant difference between the fine and coarse powder particles. Moreover, there was a higher oxygen content in the unused fine powder than in the coarse one. Although the weight percentages of elements provided by EDS may not be exact, the qualitative comparison it offers is still valid. The PSD cruves of both powder batches are also shown in Fig. 2(d). As seen in this figure, the coarse powder had a bimodal size distribution and contained more large particles (> 45 µm). In addition, more finer particles (< 20 µm) were present in the fine powder batch (12% in the fine vs. 8% in
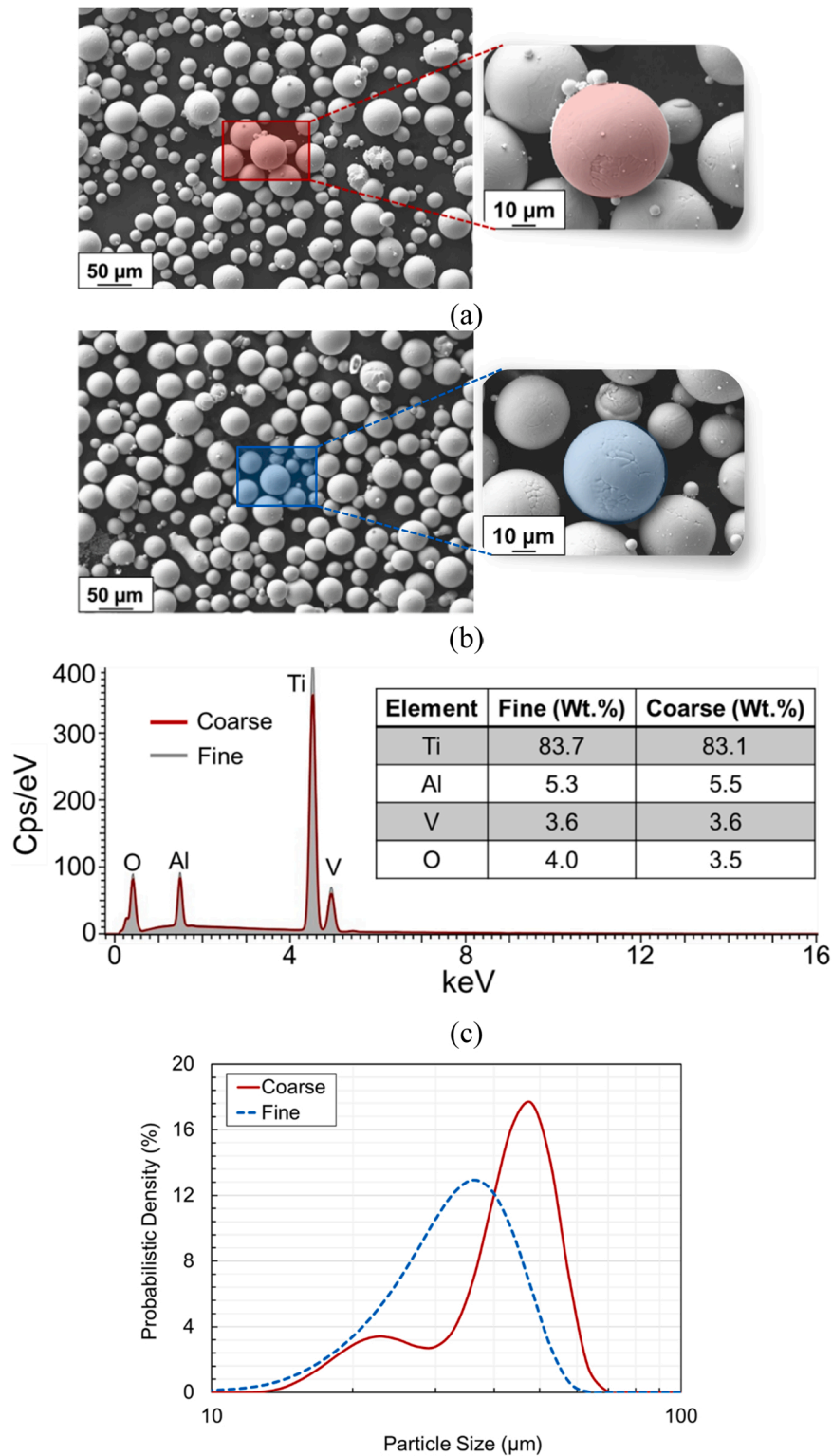
Fig. 2. Powder particles' morphology of the (a) coarse and (b) fine plasma atomized Ti64 powder batches as well as (c) the surface chemistry from shaded particles in the magnified images measured via EDS. The powder PSD curves for both batches are also shown in (d).

the coarse).

To achieve a better understanding of how the PSD and morphology can affect the powder flow behavior, the rheological properties of both powder batches were measured. A summary of all rheological properties obtained from FT4 along with their definitions is reported in Table 3. In this table, powder characteristics are given after the sieving process, as the powder that was used for the fabrication. A higher basic flowability

energy value is typically associated with lower flowability. As reported in Table 3, both powder batches have comparable basic flowability energy values after sieving, with that of the coarse powder being slightly higher. This trend correlates with the PSD spans of 0.71 and 0.76 for the fine and coarse powder batches, respectively (see Table 1). Generally, a powder with a lower span (i.e., narrower PSD) has higher flowability [5].

Table 3
A summary of powder rheological and bulk characteristics obtained in this study along with the definition of powder rheological characteristics adapted from [40].

Powder Characteristic	Fine Powder	Coarse Powder
Basic Flowability Energy (mJ)	280 ± 3.6	282.0 ± 2.5
Specific Energy (mJ/g)	1.6 ± 0.2	1.8 ± 0.1
Conditioned Bulk Density (g/mL)	2.6 ± 0.2	2.8 ± 0.0
Tapped Density (g/mL)	2.8 ± 0.0	2.9 ± 0.0
Compressibility (%)	2.6 ± 0.5	3.3 ± 0.1
Cohesion (kPa)	0.10 ± 0.00	0.10 ± 0.02
Pressure Drop (mBar)	9.5 ± 0.6	7.1 ± 0.2
Aeration Energy (mJ)	5.3 ± 0.9	5.0 ± 0.3
Definition of Powder Rheological Properties		

Basic Flowability Energy: Amount of work done while moving the blade within the powder bulk in a downward motion

Specific Energy: Amount of energy to move the blade within the powder bulk in an upward motion in an unconfined (i.e., low stress) environment as there is no constraint on top of the powder bulk

Conditioned Bulk Density: The bulk density of the powder in a low-stress condition

Tapped Density: The bulk density of the powder when it is consolidated

Compressibility: Shows the change in volume as a function of applied normal stress

Cohesion: Amount of shear stress needed to flow the powder while the applied normal stress is zero

Pressure Drop: Indicates how easily the gas can permeate the powder while is under applied compression (3 kPa) and the gas flows from below the powder bulk

Aeration Energy: Indicates how easily the powder fluidizes when it is subjected to gas flow

The specific energy, measured with basic flowability energy in the same test sequence, is also related to flowability. Since it is measured while the blade is moving upwards, specific energy represents the flowability in a low-stress environment. Specific energy values smaller than five can indicate powder with low cohesion. The very close basic flowability energy and specific energy measures of both batches indicate comparable flowabilities and cohesivity between them, which is also reflected in their identical cohesion values of 0.1 kPa.

While the fine and coarse powder batches had different PSDs, similar conditioned bulk and tapped densities were recorded, with slightly higher density values for the coarse powder batch. This was likely because powders with a wider PSD span can occupy space more efficiently and typically have higher theoretical packing densities, even though the actual powder bed density is typically lower than its theoretical packing density [41]. However, the compressibility, which measures how powder reacts to compaction under the recoater arm, of the coarse powder (3.3%) was slightly higher than the fine powder (2.6%), although both values were low. When agitated, powder particles tend to segregate into different size groups [42] (see schematic illustration provided in Fig. 3). For the coarse powder, the segregation depicted in Fig. 3 also tends to be more severe than the fine powder due to its wider PSD span, and it is more likely to contain regions of mixed particle sizes and agglomerates. As finer particles in a wide PSD powder batch typically tend to adhere to other particles due to their high surface/volume ratio and interparticle friction [4], they form agglomerates which have lower flowability and tend to create empty spaces around them. The empty spaces around these agglomerates most likely are the reason for the slightly higher compressibility of the coarse powder [4,5]. The more pronounced empty spaces within the coarse powder can form pathways of higher gas permeability which should lead to a lower pressure drop, which was indeed the case. As shown in Table 3, the coarse powder had a pressure drop of 7.1 mBar, while the fine powder
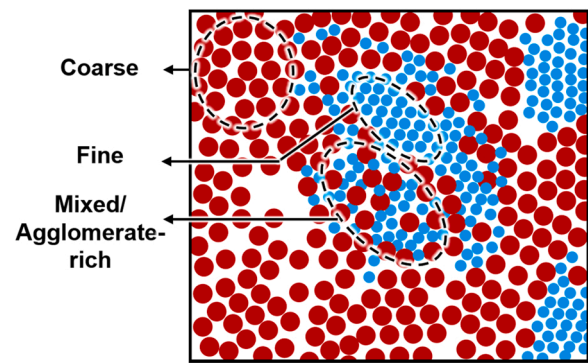

Fig. 3. Schematic illustration of the coarse powder bed particle arrangement.

had a pressure drop of 9.5 mBar.

Aeration energy is a measure of how easily the powder fluidizes when subjected to gas flow and is also relevant to the AM process. Lower aeration energy is generally desired for the PBF process to help achieve a more uniform powder bed with a higher powder bed density (PBD) and lower mechanical interlocking between powder particles [6]. Table 3 shows quite comparable aeration energies for both powder batches.

3.2. Microstructure characterization, defect distribution, and surface roughness

Upon investigation of the microstructural samples in the longitudinal plane (longitudinal direction aligned with build direction) of fabricated specimens from the coarse powder, a Widmanstätten microstructure was seen in the non-heat-treated (NHT) condition as shown by the inverse pole figure (IPF) maps in Fig. 4. Even though the characteristic cooling rate around the solidification temperature of L-PBF processes around 10^5 K/s can result in pure α' (and or α") martensites, the repeated reheating during the layer-by-layer fabrication likely have partially decomposed the martensitic phase [2]. Indeed, the EBSD scans revealed a β phase fraction of 1%, consistent with the values reported from other studies in the NHT condition [43]. No difference in phase fraction was detected between the specimens fabricated from the coarse and fine powder batches in the NHT condition. The remaining phases, occupying 99% of volume, are a mixture of α and α'(α"). Indeed, in the annealed condition, further decomposition of the martensitic phase resulted in a β phase fraction of ~29%.

Microstructures of the coarse (Fig. 4(a)) and fine (Fig. 4(b)) powder specimens in the NHT condition were obtained from the microstructural coupons placed in the East location. It is evident from the IPF maps that prior-β columnar grains are mainly elongated towards the building direction which is the primary path of heat dissipation [44]. Finally, the lath thickness was measured for the NHT and annealed coarse as well as the NHT fine conditions from the IPF maps. As seen in Fig. 4(d), the lath thickness was slightly coarser for the fine powder batch in NHT condition. The large error bars are consistent with the significant variation in the lath thickness in each condition. Additionally, the mean lath martensite thickness was seen to slightly increase from the NHT to the annealed coarse condition.

To investigate defect distribution inside the specimens before testing, two specimens were selected from each location (i.e., East and West) of each powder batch for X-ray CT. The 3D visualizations performed are presented in Fig. 5(a). Additionally, a bar chart showing the size distribution of defects normalized for a 10-mm³ sample size inside the representative gage sections is presented in Fig. 5(b). Fig. 5(b) shows that the coarse powder specimens fabricated in the West location tend to yield fewer defects in all defect size ranges than the ones fabricated in the East location. In the case of the fine powder, it appears from Fig. 5(b) that the number of defects was less in these specimens as compared to their counterparts from the coarse powder regardless of the location.
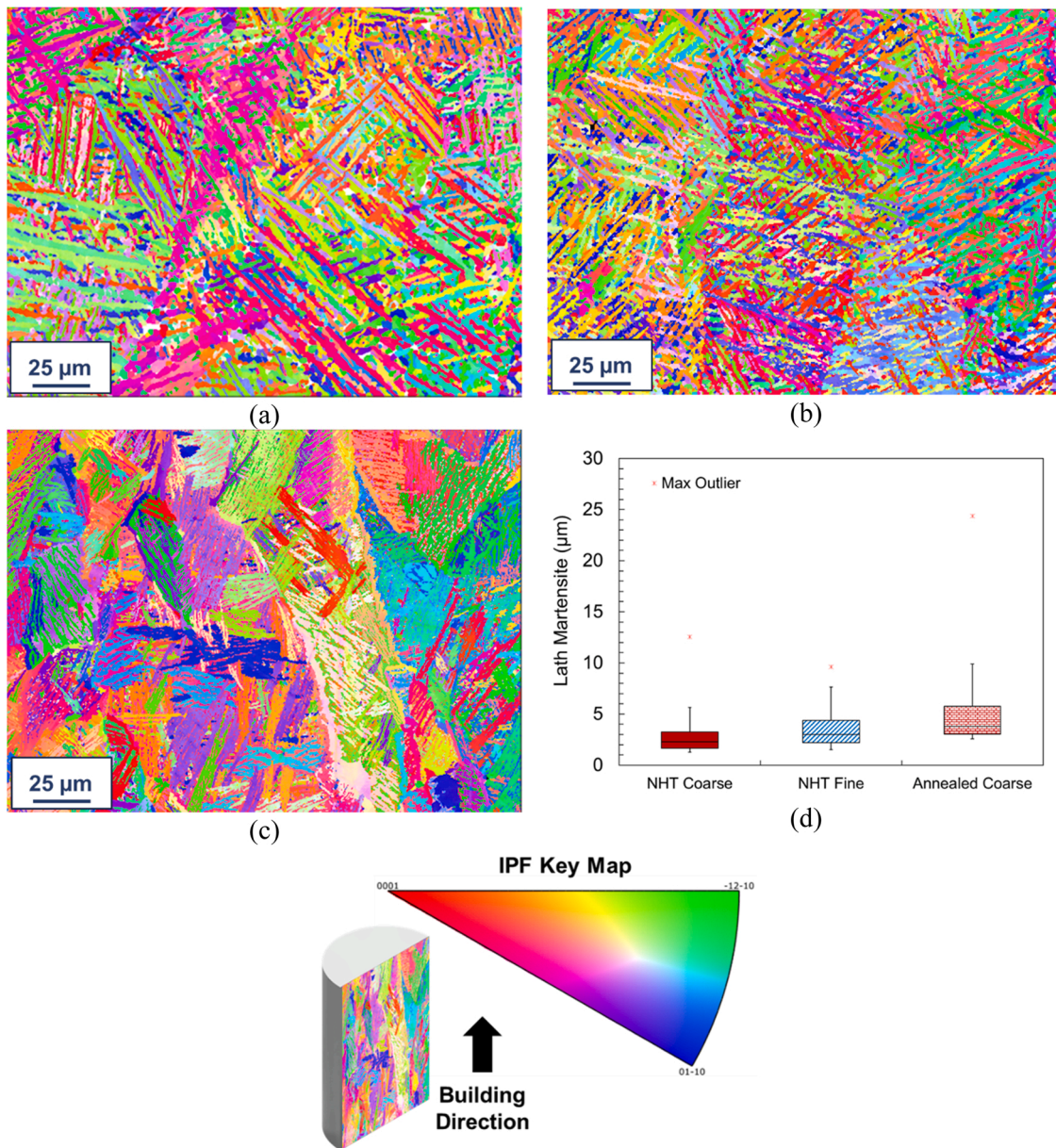
Fig. 4. Microstructure of L-PBF Ti64 for the (a) NHT coarse, (b) NHT fine, and (c) annealed coarse powder specimens along with (d) lath thickness for all the conditions.

The larger population of defects in the coarse powder specimens can be attributed to the "empty spaces" formed from the non-uniformly distributed powder and the potentially higher cooling rates when this powder batch was used for the fabrication. Coarser powder tends to have higher cooling rates due to the lower surface-to-volume ratio of the larger powder particles which reduces the energy absorption efficiency [11,17]. The total number of defects in the 10-mm^3 volume of the gage section was 18 and 12 for the coarse powder specimens in East and West, and 4 and 2 for the fine powder in East and West locations.

Some very large defects, however, were still evident in these fine powder-fabricated specimens (the maximum defect sizes in μm observed in each specimen are marked on the "≥40 μm" bar in Fig. 5(b)). The maximum volumetric defect sizes were 171 and 130 μm in the fine and 113 and 83 μm in the coarse powder specimens, depending on location. Note that the size of a volumetric defect was calculated as the diameter of the sphere with equal volume. It is also important to note that all specimens, regardless of the powder type or location, had overall densities greater than 99.99% based on the X-ray CT scans.

The surface roughness of all as-built specimens fabricated from coarse and fine powder batches in the gage sections was measured using R_a — the arithmetical mean height of line profiles. As shown in Fig. 6(a), even though the mean values of R_a showed slight variations as a function of build location as well as PSD, significant overlaps in the error bands are also evident. The specimens fabricated from the coarse powder had slightly higher surface roughness as compared to those from the fine powder which has been attributed to the higher energy density level required by coarser particles to achieve a full melting in some studies [3, 17]. In addition, the surface profiles of a coarse powder specimen and a fine powder specimen in the East location are shown in Fig. 6(b). A large amount of partially melted powder particles were seen to adhere to the surfaces of both specimens. However, they were more frequent and larger in the case of the coarse powder specimen, which further explained the higher measured surface roughness.

Within the build with fine powder, it was found that the West specimens had almost comparable surface roughness compared to the East ones. However, this location dependency of surface roughness was
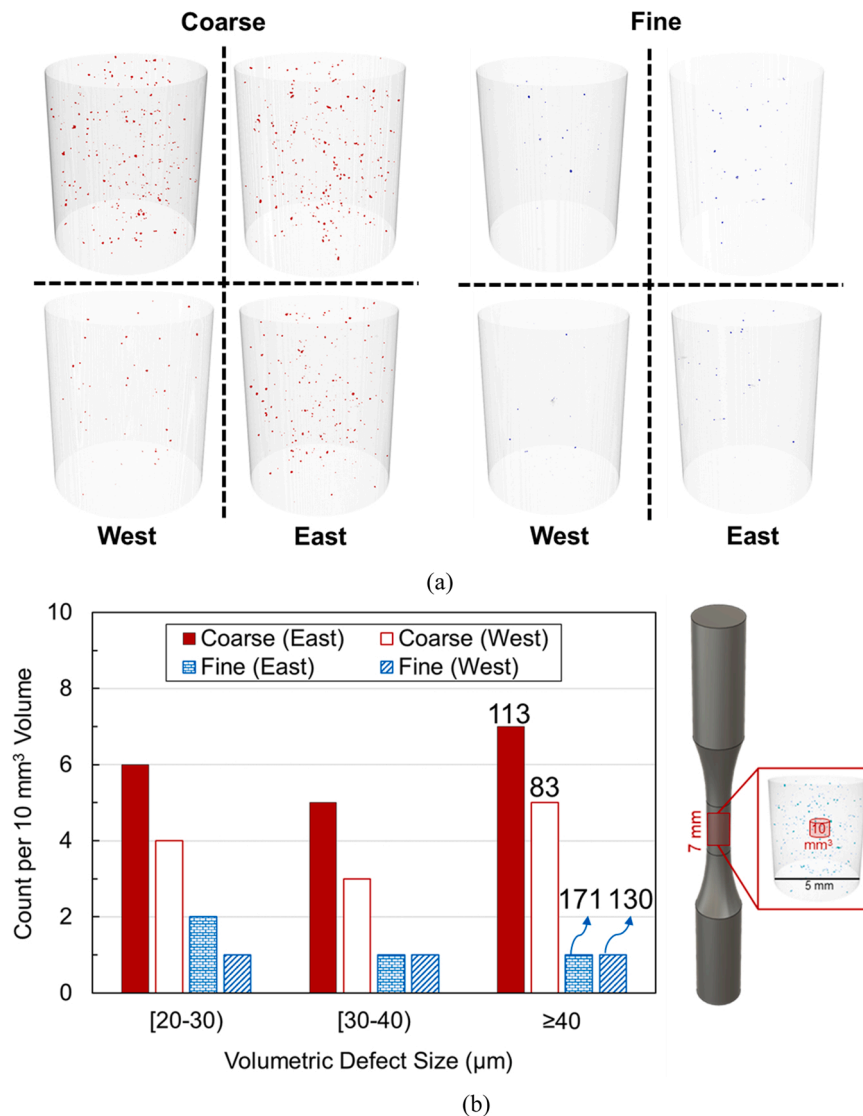
Fig. 5. 3D visualizations of defect population in the coarse (depicted by red) and fine (illustrated by blue) powder specimens placed in different locations of the build plate, and (b) histograms demonstrating the volumetric defect in 10 mm^3 sample size from the representative specimen gage sections. The maximum defect size (in μm) for each condition is labeled on the corresponding bar.

more for the specimens fabricated from the coarse powder. Such PSD-specific location dependency may be attributed to the possible segregation of finer and coarser particles given rise to the "front stress-free turning powder wedge" behavior proposed in some studies [18,20]. For instance, Jacob et al. [18] reported that during powder spreading, finer particles tend to move to the bottom of the powder bulk, and consequently, are deposited closer to the dispenser while coarser ones might deposit near the overflow bin (i.e., collector). Another possible reason may be that some of the West specimens (i.e., Southwest) were closer to the spatter-rich region in the L-PBF machine which has been shown to result in higher surface roughness values [45].

3.3. Tensile behavior

Quasi-static tensile tests were performed on both sets of specimens fabricated from coarse and fine powder batches. As explained in the experimental setup, all tensile tests were paused at 5% strain to remove the extensometer to prevent damage, as such ε_f was measured after the tensile test. In Fig. 7(a), the tensile properties, including UTS, YS, and ε_f, measured from this study as well as the minimum requirements for L-PBF Ti64 specimens fabricated vertically (i.e., along the Z-axis) based on

ASTM F2924 [46] are provided. Concerning the location, it seems that tensile properties including UTS, YS, and ε_f are independent of location on the build plate.

Regarding the effects of particle size on the tensile properties, it can be seen from Fig. 7(a) that there were negligible changes in UTS and YS between the specimens manufactured from fine and coarse powder batches. This behavior can be correlated well with the similar microstructure that was seen in the specimens fabricated from both batches. However, the ε_f in fine powder specimens was lower than the coarse powder specimens which might be due to the larger maximum defect sizes in fine powder specimens (see Fig. 5(b)) and the higher oxygen content in the fine powder (see Fig. 2). While a higher strength might be expected due to higher content of oxygen in fine powder, almost comparable strength was noted which can be attributed to the strengthening effect of slightly thinner lath martensite in the coarse powder [47,48]. The engineering stress-displacement behavior is also shown in Fig. 7(b) and (c) for the specimens tested from the East and West locations.

3.4. Fatigue behavior & failure analysis

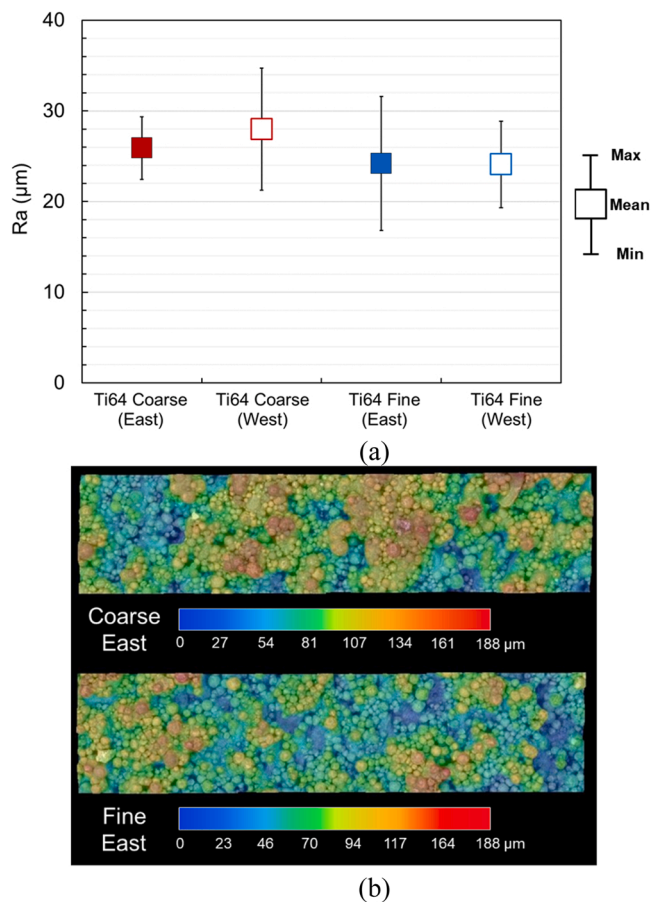The axial fatigue behaviors of both as-built and machined specimens

Fig. 6. (a) R_a values for the specimens manufactured from the coarse and fine powder batches in East and West locations, and (b) surface profile micrographs for a coarse and a fine powder specimen located in the East.

from different locations on the build plate and fabricated from coarse and fine powder batches are presented in Fig. 8. It is evident from Fig. 8 (a) that the difference between the fatigue lives of as-built specimens fabricated from both batches is relatively small in the MCF ($\leq 10^5$ reversals to failure) and HCF ($>10^5$ reversals to failure) regimes. In addition, regardless of the powder type, it seems that the West as-built specimens have slightly lower fatigue resistance compared with the East as-built ones in the HCF regime.

In the machined condition (see Fig. 8(b)), it was seen that the coarse powder specimens have higher fatigue resistance as compared to fine powder specimens in the MCF regime. This behavior was following the observations reported in [10], which can be attributed to the higher ductility of the coarse powder specimens. In low-cycle fatigue (LCF) and MCF regimes (i.e., higher stress levels), crack growth accounts for a more significant portion of the overall fatigue life [49]. Therefore, the higher ductility of the coarse powder specimens may imply higher fracture toughness and larger crack size at fracture which typically increases the crack growth life. At the lower stress level (i.e., 400 MPa), the coarse powder specimens still appear to outperform the fine powder ones (note the three runouts in coarse condition vs. no runouts in fine condition) despite the more significant data overlap. This is consistent with the observation that the largest defects in the fine powder specimens being larger than those in the coarse powder ones, although in general more volumetric defects were detected in coarse specimens. In addition, increasing scatter in data was noticed with decreasing stress levels, which can be ascribed to the more prominent effect of defects in these conditions [5,12,50]. As to location dependency in the machined specimens, no apparent trend was seen between the fatigue lives of East and West specimens manufactured from either powder batches. A

summary of all force-controlled fatigue tests is reported in Table 4.

While fracture surfaces of all specimens were characterized from the digital optical microscope, only a few notable fractography images were presented in this article (see Fig. 9 and Fig. 10). Fig. 9(a), (b), and (c) present fracture surfaces of as-built specimens tested at $\sigma_a = 300$ MPa and a frequency of 4 Hz for the coarse powder in East and West as well as the fine powder in East, respectively. As seen in these figures, cracks initiated in multiple locations in each specimen from the rough surfaces of both coarse and fine powder specimens in East and West locations, resulting in similar fatigue lives within the range of 80,398 and 104,584 reversals to failure. It is well established that rough surfaces of AM parts, which are mainly derived from partially-melted powder particles and the stair effect due to the layer-by-layer fabrication, can behave like micro notches [51]. These micro notches on the surface can drastically deteriorate the fatigue resistance of AM parts when they are subjected to cyclic loading conditions.

In the machined condition, however, as the surface micro notches are removed, cracks mainly start from the internal or near-surface volumetric defects (i.e., gas-entrapped pores and lack-of-fusion defects). Fig. 10(a)-(d) shows the fracture surfaces of the coarse and fine powder specimens from the East and West locations and tested at $\sigma_a = 500$ MPa. It is evident that cracks initiated from near-surface gas-entrapped pores in the two coarse powder specimens in East and West with fatigue lives of 201,716 and 155,384 reversals to failure, respectively. The equivalent defect size (i.e., $\sqrt{area}$ μm) was also calculated based on Murakami's principles [52], and it is labeled on each image. Unlike the coarse powder specimens, in the fine powder ones, cracks mainly initiated from internal defects (see Fig. 10(c)-(d)). Although these defects were farther away from the surface of the specimens, the defect sizes were appreciably larger than the coarse powder specimens, resulting in fatigue lives of 165,706 and 136,838 reversals to failure in the East and West specimens, respectively.

4. Discussion on experimental results

4.1. Effect of powder characteristics on the surface and volumetric defects

On average, the coarse powder specimens had slightly higher R_a values as compared to the fine powder specimens (see Fig. 6(a)). The higher R_a values of the coarse powder specimens can be explained by the existence of larger particles in the coarse batch, which typically have a lower absorptivity. Therefore, particles on the surface may not completely melt resulting in a higher surface roughness [17] (see Fig. 6 (b)). Concerning the effects of part location, it was noted that the coarse powder specimens located in the West had generally higher R_a values as compared to the East ones. However, this difference was less obvious for the fine powder specimens due to its slightly lower mechanical interlocking (i.e., lower specific energy and basic flowability energy) and consequently better flowability, and more uniform powder bed [6]. In addition, the narrower PSD span of the fine powder could also reduce the severity of particle size segregation during spreading.

As evident in Fig. 5(a) and (b), the coarse powder specimens contained a higher number of defects though the maximum defect size for fine powder specimens was larger. The higher defect population in the coarse powder specimens could have been derived from multiple factors. First, the coarse powder had an inferior packing state as compared with the fine powder batch due to its more severe powder size segregation. Therefore, when the regions of low packing densities in the coarse powder batch are melted, porosity is more probable to form. This is exacerbated by the fact that coarser particles require more input energy to completely melt [17] due to their lower absorptivity [53] associated with their lower surface-to-volume ratio. Effectively, when the regions of coarser particles in the powder bed are melted, the cooling rate is higher, leading to the formation of more defects [54].

Interestingly, the maximum defect sizes detected by the X-ray CT were 130–171 μm in the fine and 83–113 μm in the coarse powder
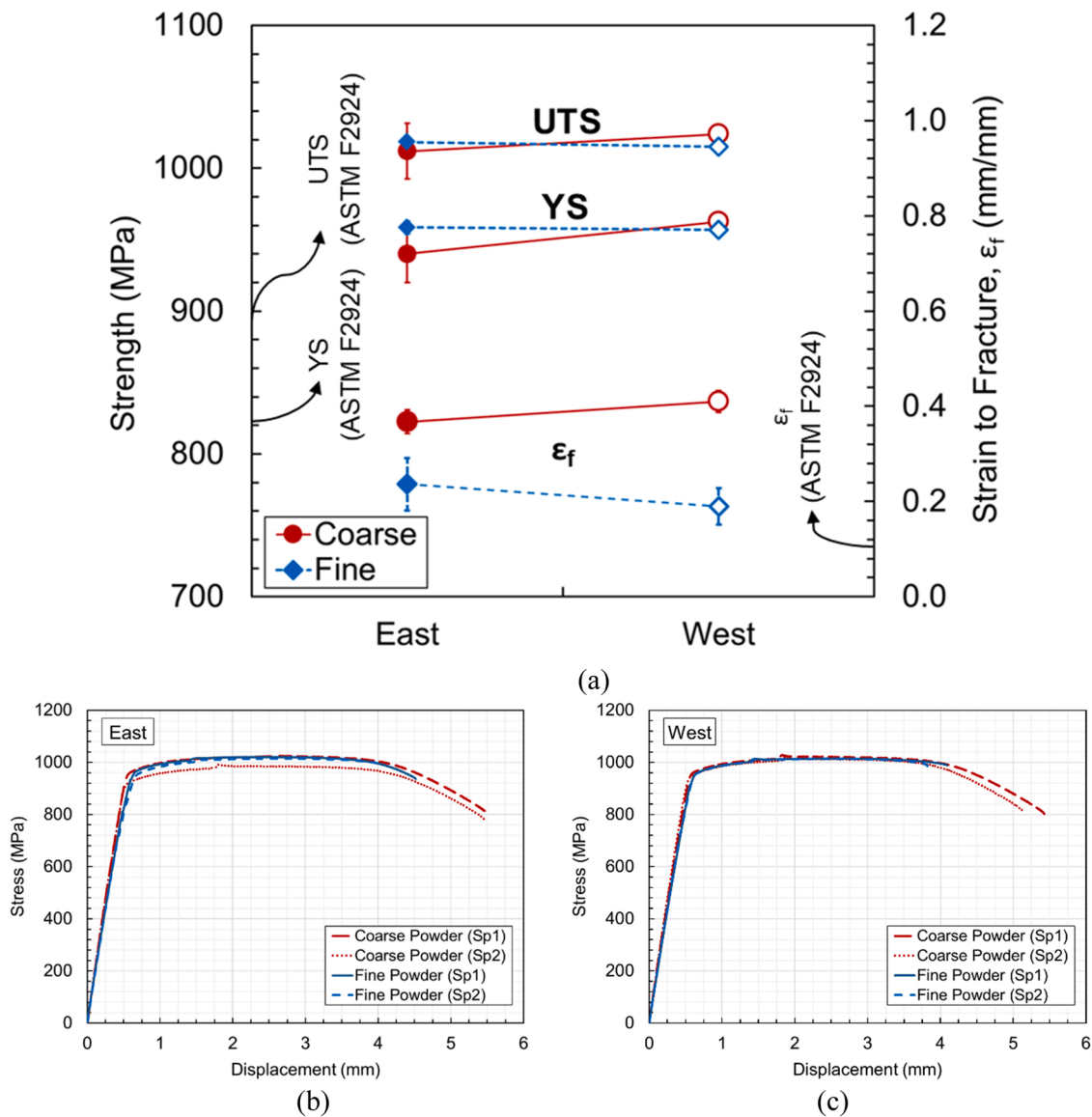
Fig. 7. (a) Quasi-static tensile properties of L-PBF Ti64 specimens fabricated from coarse and fine powder batches and different locations along with the minimum requirements according to ASTM F2924. All specimens have been annealed prior to testing. Since only two tensile tests were performed per condition, the two ends of an "error" bar represent the two measurements of a property for a given location and powder batch, while the markers represent the mean values and (b) and (c) engineering stress-displacement curves for both fine and coarse powder batches in the East and West, respectively.

specimens. Observing larger-sized defects in the fine powder specimens which possessed a superior packing state was rather surprising. The presence of substantially large defects in the fine powder specimens appears to be the result of spattering. Indeed, the crack initiation sites in the fatigue specimens and fracture nucleation sites of the tensile specimens fabricated from the fine powder were rich in Si, which could have been induced by spatters resulting in the formation of large pores (see Fig. 11). The Si is often added to Ti64 to enhance its resistance to oxidation and creep, as well as to increase its tensile strength [55,56]. The Si-rich regions in Ti64 tend to form a mixture of $TiSi_x$, TiO_2, and SiO_2 phases [57]. Among the compounds, the melting point of $TiSi_x$ is substantially lower than Ti (liquidus temperature of 1330 °C for Ti-Si alloy compared to 1670 °C for Ti); besides, the SiO_2 phase has a decomposition temperature of only 1861 °C in oxygen lean environments (similar to the build chamber which is purged in argon) [58] (note that the boiling point for Ti is over 3200 °C). When interacting with laser, the Si-rich powder particles would likely melt early, and the contained SiO_2 phase rapidly decompose into Si and gaseous O_2. The explosive formation of the gaseous O_2 within the melted Si-rich powder

particles was likely the cause of the Si-rich spatters observed within the specimens. Both batches had approximately the same level of Si, yet the fine batch had higher oxygen pickup due to the higher surface-to-volume ratio. The higher oxygen content in the fine powder most likely had formed more SiO_2, which results in more spatter in the fine powder specimens. Indeed, other possible factors may also exist resulting in the observation of larger defects in the case of fine powder which necessitates further investigations.

Concerning the effects of location, it was observed that the number of defects in the specimens manufactured from the coarse powder and placed in the West was, to some extent, lower as compared to their counterparts located in the East. Such location dependency of defect population may be attributed to the possible segregation of finer and coarser particles by spreading, i.e., the "front stress-free turning powder wedge" behavior proposed in some studies [18,20] and somewhat lower flowability of the coarse powder. Finer particles tend to be deposited closer to the dispenser, while coarser ones can be spread further due to their wider PSD, resulting in the formation of more loosely packed regions in the East. In contrast, the fine powder specimens located in the
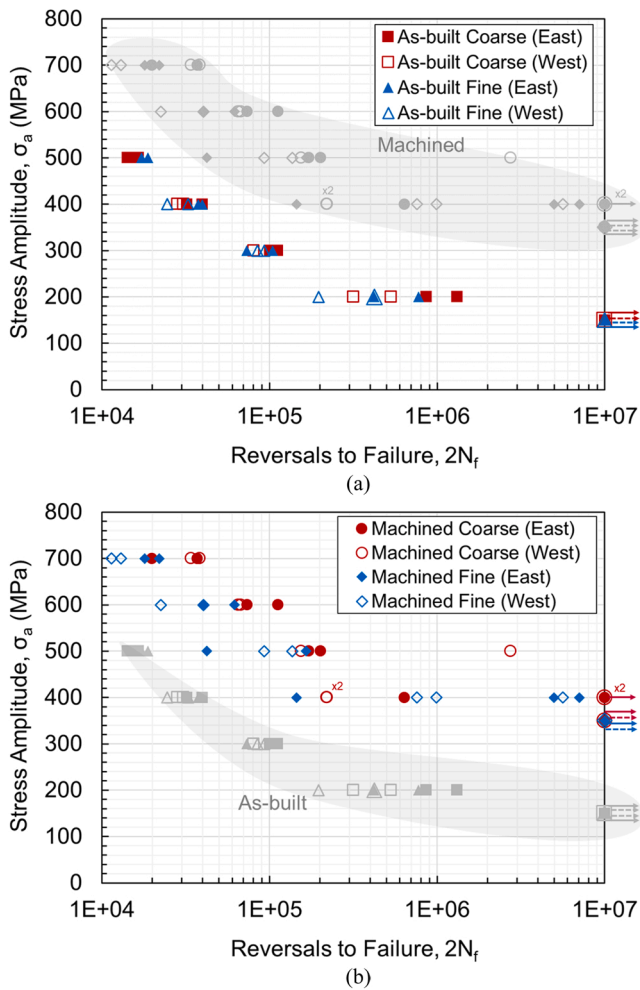
Fig. 8. Fatigue performance of L-PBF Ti64 specimens fabricated from coarse and fine powder batches from the East and West locations in their (a) as-built and (b) machined surface conditions. All specimens have been annealed before testing. The grayed-out markers in each subfigure represent the opposing surface condition for each comparison (i.e., machined in (a) and as-built in (b)).

East and West had almost similar number of defects, which could be ascribed to its more uniform PSD (i.e., lower span) and consequently, the higher powder flowability.

4.2. Effect of powder characteristics on tensile behavior

As seen in Fig. 7, the coarse and fine powder specimens had comparable UTS and YS. Tensile YS is primarily governed by the microstructure of the parts and is not expected to be different between the specimens fabricated from the two powder batches as there were no significant changes in the microstructure (see IPF maps shown in Fig. 4). In addition, since Ti64 is well known for its low strain hardenability, the UTS is typically not much higher than the YS and is not sensitive to ductility. In terms of ductility, it was observed that the coarse powder specimens possess superior ε_f which is consistent with the observations reported in [10,17]. The lower ductility of fine powder specimens can be attributed to the presence of larger volumetric defects due to spattering and their higher oxygen content which likely have increased the material's sensitivity to defects.

Fracture surfaces of the tensile specimens, presented in Fig. 12, revealed different fracture mechanisms for the coarse and fine powder specimens, with the former being ductile and the latter being brittle. The fracture of the coarse powder specimens occurred after the onset of necking and its surface resembles the classic cup and cone feature, which

Table 4
A summary of fully-reversed ($R_\sigma = -1$) force-controlled fatigue tests for L-PBF annealed Ti64 specimens in both as-built and machined surface conditions.

Specimen ID	σ_a (MPa)	2 N_f - Fine (Reversals)	2 N_f - Coarse (Reversals)	Location	Surface Condition
019	400	24,538	30,634	West	As-built
008	400	32,712	28,332		
009	300	92,984	80,398		
106	300	84,678	N/A		
010	200	196,858	316,330		
017	200	422,610	532,308		
018	150	10,000,000	10,000,000		
087	500	17,284	14,250	East	
034	500	18,822	16,524		
042	400	39,650	39,856		
077	400	37,628	32,170		
043	300	73,322	111,686		
078	300	104,584	100,376		
033	200	420,944	1,318,620		
086	200	773,836	862,818		
079	150	10,000,000	10,000,000		
044	150	10,000,000	10,000,000		
104	700	11,388	38,324	West	Machined
011	700	12,996	34,098		
014	600	40,338	67,876		
112	600	22,510	65,350		
110	500	93,098	2,744,548		
012	500	136,838	155,384		
013	400	757,194	219,854		
111	400	990,378	220,690		
098	400	5,630,226	10,000,000		
015	350	10,000,000	10,000,000		
037	700	21,996	37,250	East	
085	700	17,992	19,958		
038	600	40,142	112,776		
082	600	61,686	73,630		
040	500	165,706	201,716		
084	500	42,282	172,172		
039	400	4,992,374	10,000,000		
083	400	145,146	639,024		
076	400	7,049,054	10,000,000		
044	350	10,000,000	10,000,000		

had a fibrous central region surrounded by an annular shear lip (see Fig. 12(a)). The fibrous region is the result of the nucleation, growth, and subsequent coalescence of the voids during the tensile loading driven by the hydrostatic tension in the neck. Some of the voids were nucleated in a homogenous fashion and appeared as dimples on the fracture surface. Others grew from volumetric defects which are indicated by black arrows in Fig. 12(a).

In contrast to the coarse powder specimens, the fracture of the fine powder specimens occurred without clear evidence of necking and under a different mechanism. As shown in Fig. 12(b), the fracture surface lacked a central symmetry and featured a central flat region that was open to the specimen's external surface from one side. Relatively large defects, such as the one indicated by the yellow arrow in Fig. 12(b), were always observed at the opening. The flat region was partially surrounded by the shear lips. Closer inspection also revealed that the river marks [59] on the flat regions converged toward its opening to the specimen surface, suggesting the opening to be the initiation site for fracture. The initiation of fracture was likely due to the close interaction between the defect (indicated by the yellow arrow in Fig. 12(b)) and the specimen surface. The flat region is the plane strain portion of the unstable propagation of the tensile crack, while the shear lip is the plane stress portion. Occasionally, a large defect could be found in the interior of the fracture surface residing either on a "plateau" or in a "basin" (see Fig. 12(b)). In such cases, although secondary cracks initiated from these internal defects, their propagation was suppressed by the main crack. These defects did not reside on the same plane with the main crack, therefore the secondary cracks formed plateaus/basins when they joined with the main crack.
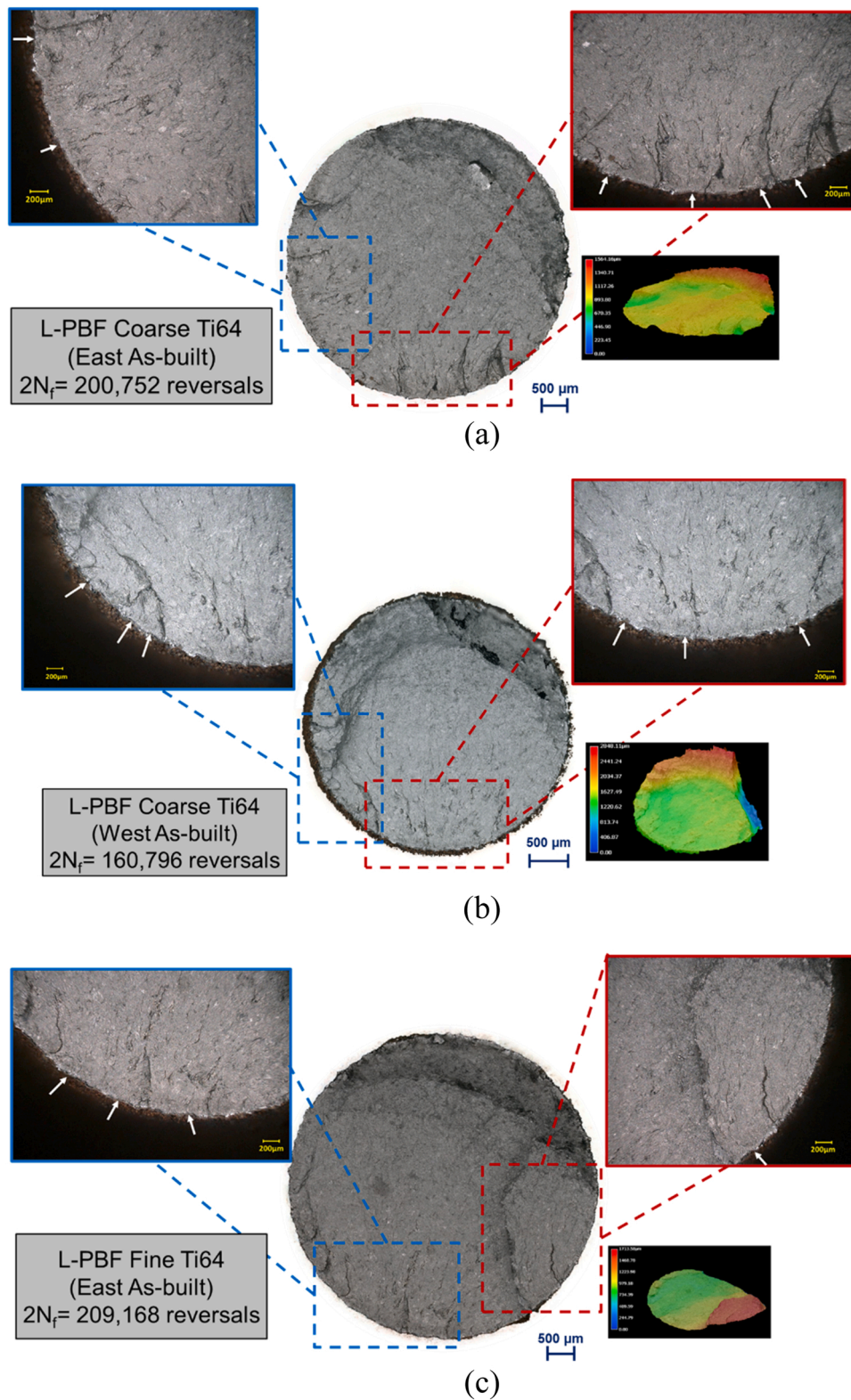
Fig. 9. Fracture surfaces of L-PBF annealed Ti64 specimens in their as-built surface conditions for the coarse powder specimens in (a) East and (b) West, as well as (c) fine powder specimen in the East. All specimens were tested at σ_a= 300 MPa. Crack nucleation sites are indicated with white arrows.

The difference in the fracture mechanisms in the two specimen batches is likely due to the different defect and oxygen contents. In coarse powder specimens, the maximum size of the defects was significantly smaller and the oxygen fraction was lower than those in the fine powder specimens. Therefore, even though the number of defects per volume was higher than that of the fine powder specimens, the surface cracks formed due to the near-surface defects in coarse specimens, if any, did not have sufficient stress intensity factors under loading to induce fracture. This permitted necking and resulted in the typical ductile fracture. Conversely, the much larger although fewer defects in
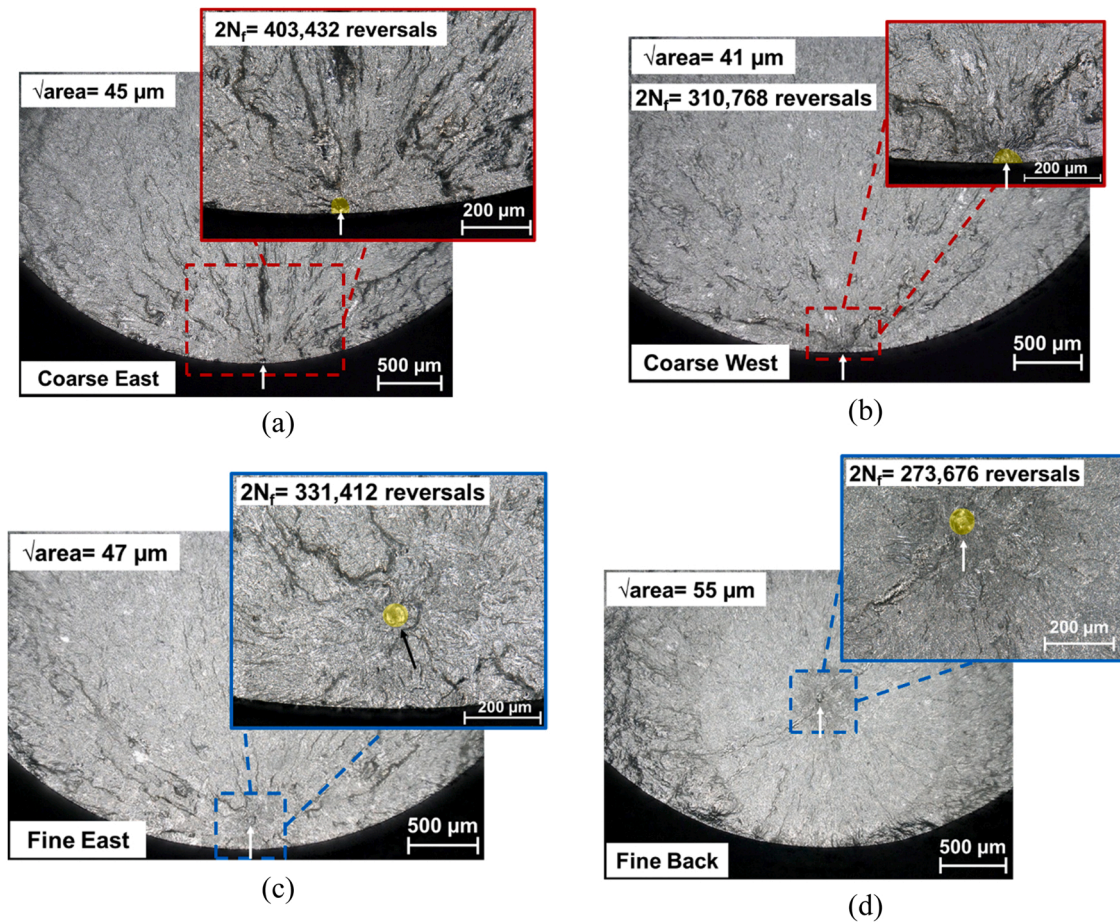
Fig. 10. Fractures surfaces of L-PBF annealed Ti64 specimens in the machined surface condition for the coarse powder specimens in (a) East and (b) West, as well as the fine powder specimens in (c) East and (d) West. All specimens were tested at σ_a= 500 MPa. In these images, the crack initiation sites are also portrayed with yellow shade in the magnified views. Arrows are also placed toward the crack initiating defects in all images.

the fine powder specimens (where the oxygen content was higher) formed cracks that were large enough to induce surface-originated, brittle mode fracture. Despite the low number of defects per volume, the probability of finding a large defect near the specimen surface was still relatively high.

4.3. Effect of powder characteristics on fatigue behavior

When the fatigue performance of specimens in their as-built surface condition was investigated, negligible changes between the coarse and fine powder specimens were noted (see Fig. 8(a)). This observation was following the R_a results which showed almost identical values for both batches (see Fig. 6(a)). In the case of location, some improvement in fatigue resistance of as-built coarse specimens located in the East was seen as compared with the ones in the West in the HCF regime ($\geq 10^5$ reversals to failure), which was consistent with the higher R_a of coarse powder specimens in the West location. The higher fatigue resistance of coarse powder specimens in the East can be attributed to the more prominent effects of surface roughness in the HCF regime [49]. The similar trend was less pronounced for the fine powder due to its slightly higher flowability, which also agreed with the R_a results in Fig. 6(a). Regardless of the powder and the location, cracks initiated from the surface of as-built specimens, resulting in final fatigue failures (see Fig. 9).

In the machined surface condition, a higher fatigue resistance was generally observed for the coarse powder specimens (see Fig. 8(b)), which was more discernible at higher stress levels, i.e., $\sigma_a \geq 500$ MPa. The fatigue lives on these stress levels are mostly in the MCF regime,

where the crack propagation stage occupies a significant portion of the total fatigue life. The coarse powder specimens provided slightly better ductility which may be beneficial for their MCF resistance. At lower stress levels (such as $\sigma_a = 400$ MPa), the advantage of the coarse powder specimens became less clear. Nevertheless, it is still important to note the two coarse powder specimens from the East and one from the West reached run-out at this stress level, while none of the fine powder specimens did. In the HCF regime (such as at the stress level of $\sigma_a = 400$ MPa), fatigue life is governed by crack initiation which often occurs at defects. The reason for the significant overlap in fatigue data at this stress level may be explained by the uncertainty in the maximum defect size in each specimen. This is evident from the defect size (measured by $\sqrt{area}$ μm) reported in Fig. 10, where both larger and small fatigue critical defects could present in either batch of specimens even though those in fine specimens were generally larger.

To formally assess the uncertainty in the size of crack initiating defects in both batches of specimens, $\sqrt{area}$ for these defects projected onto the loading plane was measured from the fracture surfaces following Murakami's approach [52], and its distribution was analyzed using extreme value statistics [2,60]. Since only the information of crack initiating defects were involved in the analyzes, the outcome could shed light on the size ($\sqrt{area}$) of the most detrimental defects within a batch of specimens [61]. Although the analysis was performed on fatigue specimens, the knowledge can provide insights towards the statistics of extreme defects in larger components fabricated with the same process parameters, as long as the surface to volume ratio is similar [2]. Gumbel distribution, which was shown to describe the size distribution of extreme defects well [2], has been adopted in this study following the
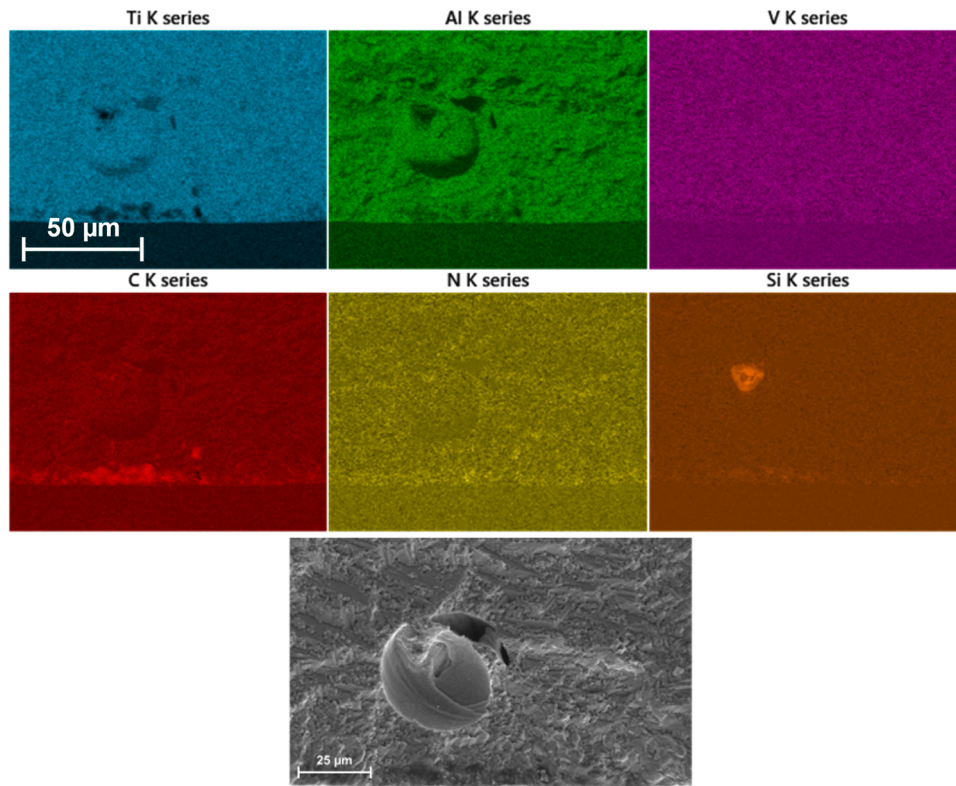
Fig. 11. EDS maps on the fracture surface of an L-PBF annealed Ti64 specimen manufactured from the fine powder.
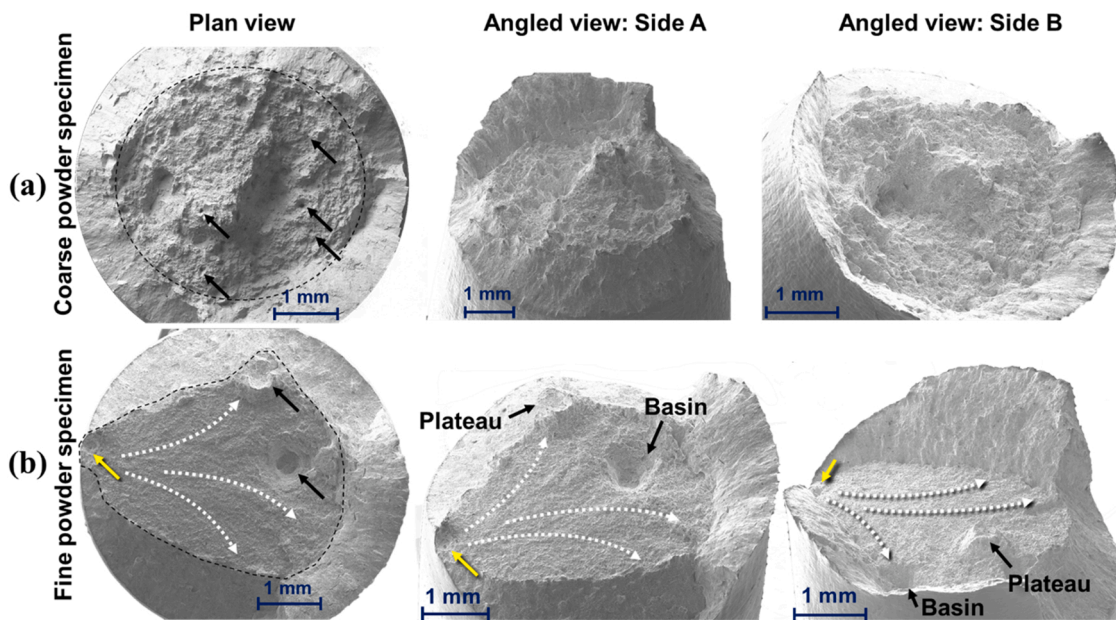

Fig. 12. Fracture surfaces of L-PBF annealed Ti64 tensile specimens in the (a) coarse and (b) fine powder specimens. Black arrows indicate the location of pores, while the yellow arrow in (b) points to the defect responsible for the onset of fracture for the fine powder specimen. The white dashed arrows in (b) mark the direction of fracture.

approach established in Refs. [61,62].

The empirical cumulative distribution functions (ECDF) for all crack initiating defects for both fine and coarse powder specimens in machined conditions are shown in Fig. 13(a) according to the extreme value statistics by Gumbel [61–64]. Note here that all of these defects were volumetric ones which were ranked according to their $\sqrt{area}$ from small to large. As shown, the Gumbel ECDF is presented as the reduced variate:

$$Y_i = -\ln(-\ln(F_i)) \tag{1}$$

where $F_i = i/N + 1$, with i being the rank of the current crack initiating defect, and N is the total number of crack initiating defects identified in each specimen batch (there were only one or a few of these defects per specimen). If the relation between the $\sqrt{area}$ and the reduced
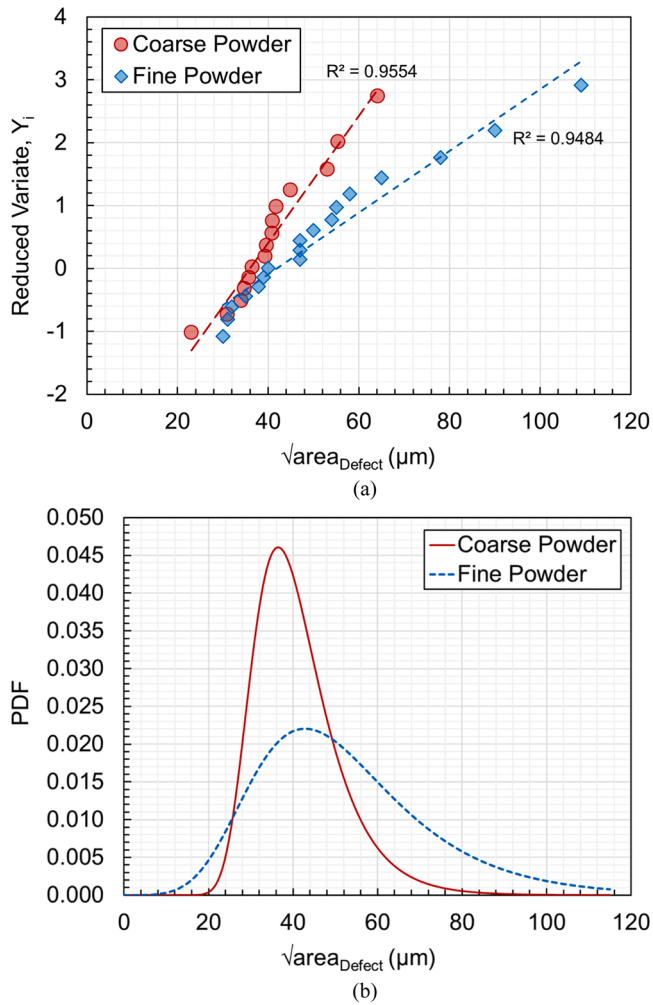
Fig. 13. (a) Estimation of the largest extreme value distribution and (b) probability density function (PDF) for crack initiating defects based on Gumbel's extreme value statistics and Murakami's $\sqrt{area}_{Defect}$ approach [52] in coarse and fine powder specimens.

variate Y_i is linear, then the distribution follows the Gumbel distribution. Agreeing with the literature [2,10,65], Fig. 13 (a) shows that the size distribution of crack initiating defects well obeys the Gumbel distribution ($R^2 = 0.9554$ and 0.9484 for coarse and fine powder specimens, respectively), whose cumulative distribution function is given as [60]:

$$F\left(\sqrt{area}\right) = \exp\left(-\exp\left(-\frac{\sqrt{area} - \lambda}{\delta}\right)\right) \qquad (2)$$

where λ and δ are the location and scale parameters of the extreme value distribution. The location parameter (λ) gives the $\sqrt{area}$ value that corresponds to the peak of the corresponding probability density distribution (PDF) function, which is given as [60]:

$$G\left(\sqrt{area}\right) = \frac{1}{\delta}[\exp(-\frac{\sqrt{area} - \lambda}{\delta})] \times \exp\left[-\exp\left(-\frac{\sqrt{area} - \lambda}{\delta}\right)\right] \qquad (3)$$

The scale parameter (δ) represents the spread of data, i.e., larger δ corresponds to wider distribution, and is used to "scale" the standard Gumbel distribution to best fit a data set. The location and scale parameters in the Gumbel distribution functions are given in Table 5 for both coarse and fine specimens. As seen in Fig. 13(a), the largest crack initiating defects in the coarse and fine powder specimens were 64 and 109 μm, respectively. In addition, the corresponding probability distribution functions (PDFs) are shown in Fig. 13(b). As shown, 90% of

Table 5
Location (λ) and scale (δ) parameters of the Gumbel's extreme value distribution obtained based on the $\sqrt{area}$ of the projected defects onto the loading plane from the fracture surfaces.

Gumbel Distribution Function Parameters	Fine Powder	Coarse Powder
Location Parameter, λ	42.9	36.4
Scale Parameter, δ	16.7	8.0

defects in coarse powder specimens were smaller than 54 μm whereas they were smaller than 80 μm in fine powder specimens. The statistical analysis confirmed the speculation made above that, going from the coarse powder to the finer powder, the size of crack initiating defects increases. However, the most probable ranges of the crack initiating defect size from the coarse and fine powder specimens significantly overlap, which can explain the fatigue results observed for the machined specimens at $\sigma_a = 400$ MPa. Although the precise fitting parameters shown in Table 5 may slightly vary depending on the population of the critical defects analyzed—fitting parameters are generally more reliable with larger population—the observations made above are nevertheless valid since each specimen set contained > 15 analyzed defects (see Fig. 13(a)).

5. Conclusions

In this study, plasma atomized Ti64 powder batches with PSDs of 15–45 μm and 15–53 μm were used to investigate the effects of particle size on the mechanical performance of parts fabricated by the L-PBF AM technique. Parts were fabricated in different locations on the build plate to study the location dependency of mechanical properties. Overall, slightly higher ductility and fatigue resistance were observed for the specimens manufactured from the coarse powder. Additional conclusions based on the experimental results can be drawn as:

- No difference in the fatigue performance of specimens in the as-built surface condition was noted due to different powder PSDs. In all as-built specimens, fatigue failures initiated from the micro notches on the surface.
- More defects were seen in the coarse powder specimens due to the inferior packing state and lower heat absorptivity of coarser powder particles. However, the maximum defect size was still larger in the fine powder specimens, which was ascribed to the powder spattering during the fabrication.
- Negligible changes were noted in the YS and UTS resulting from the similar microstructure in the coarse and fine powder specimens. Ductility, however, was larger in the coarse powder specimens as they had generally smaller defects.
- Higher fatigue resistance was observed for the coarse powder specimens which was correlated with the higher ductility and smaller-sized defects affecting the MCF and HCF regimes, respectively. While the fatigue life is majorly spent in the crack growth regime at higher stress levels, the crack initiation often dominates the fatigue life at longer life regimes.
- The largest prospective defect size assessed by the Gumbel distribution showed an increase in defect size using the fine powder compared to the coarse one. In addition, 50% of the critical defects in the specimens manufactured from both powder batches had somewhat comparable sizes.

To summarize, it was observed that powder rheological analyses are capable of interpreting and predicting the fatigue behavior of AM parts manufactured from powder batches with different PSDs. In addition, it was noticed that the coarse powder, which showed an inferior packing state compared to the fine batch can still result in almost comparable mechanical properties, and even superior ductility, as well as fatigue resistance in the MCF and HCF regimes. This shows that by carefully

selecting the appropriate PSD, it is feasible to improve the part performance. On the other hand, using a less expensive powder with larger and wider particle size distribution may not affect the mechanical performance of the AM parts; however, this observation may be material and AM system dependent.

CRediT authorship contribution statement

Arash Soltani-Tehrani: Conceptualization, Methodology, Validation, Formal analysis, Data curation, Investigation, Writing – original draft, Visualization. **Mahdi Habibnejad-Korayem:** Conceptualization, Resources, Validation, Writing – review & editing. **Shuai Shao:** Conceptualization, Methodology, Validation, Formal analysis, Data curation, Investigation, Writing – review & editing. **Meysam Haghshenas:** Conceptualization, Validation, Writing – review & editing. **Nima Shamsaei:** Conceptualization, Methodology, Resources, Formal analysis, Investigation, Writing – review & editing, Supervision, Project administration.

Declaration of Competing Interest

The authors declare that they have no known competing financial interests or personal relationships that could have appeared to influence the work reported in this paper.

Acknowledgments

References

[1] N. Shamsaei, A. Yadollahi, L. Bian, S.M. Thompson, An overview of direct laser deposition for additive manufacturing; Part II: Mechanical behavior, process parameter optimization and control, Addit. Manuf. 8 (2015) 12.

[2] J.W. Pegues, S. Shao, N. Shamsaei, N. Sanaei, A. Fatemi, D.H. Warner, P. Li, N. Phan, Fatigue of additive manufactured Ti-6Al-4V, part I: the effects of powder feedstock, manufacturing, and post-process conditions on the resulting microstructure and defects, Int. J. Fatigue 132 (2020), 105358.

[3] A.T. Sutton, C.S. Kriewall, M.C. Leu, J.W. Newkirk, Powder characterisation techniques and effects of powder characteristics on part properties in powder-bed fusion processes, Virtual Phys. Prototyp. 12 (2017) 3–29.

[4] J.H. Tan, W.L.E. Wong, K.W. Dalgarno, An overview of powder granulometry on feedstock and part performance in the selective laser melting process, Addit. Manuf. 18 (2017) 228–236.

[5] A. Soltani-Tehrani, J. Pegues, N. Shamsaei, Fatigue behavior of additively manufactured 17-4 PH stainless steel: The effects of part location and powder re-use, Addit. Manuf. 36 (2020), 101398.

[6] S.E. Brika, M. Letenneur, C.A. Dion, V. Brailovski, Influence of particle morphology and size distribution on the powder flowability and laser powder bed fusion manufacturability of Ti-6Al-4V alloy, Addit. Manuf. 31 (2020), 100929.

[7] R.M. German, Powder metallurgy science, Metal Powder Industries Federation, 1984.

[8] L. Cordova, T. Bor, M. de Smit, M. Campos, T. Tinga, Measuring the spreadability of pre-treated and moisturized powders for laser powder bed fusion, Addit. Manuf. 32 (2020), 101082.

[9] M. Salarian, H. Asgari, M. Vlasea, Pore space characteristics and corresponding effect on tensile properties of Inconel 625 fabricated via laser powder bed fusion, Mater. Sci. Eng. A 769 (2020), 138525.

[10] Z.M. Jian, G.A. Qian, D.S. Paolino, A. Tridello, F. Berto, Y.S. Hong, Crack initiation behavior and fatigue performance up to very-high-cycle regime of AlSi10Mg fabricated by selective laser melting with two powder sizes, Int. J. Fatigue 143 (2021), 106013.

[11] K. Riener, N. Albrecht, S. Ziegelmeier, R. Ramakrishnan, L. Haferkamp, A. B. Spierings, G.J. Leichtfried, Influence of particle size distribution and morphology on the properties of the powder feedstock as well as of AlSi10Mg parts produced by laser powder bed fusion (LPBF), Addit. Manuf. 34 (2020), 101286.

[12] P.E. Carrion, A. Soltani-Tehrani, N. Phan, N. Shamsaei, Powder recycling effects on the tensile and fatigue behavior of additively manufactured Ti-6Al-4V parts, JOM 71 (2019) 963–973.

[13] P. Nandwana, M.M. Kirka, V.C. Paquit, S. Yoder, R.R. Dehoff, Correlations between powder feedstock quality, in situ porosity detection, and fatigue behavior of Ti-6Al-

[14] 4V fabricated by powder bed electron beam melting: a step towards qualification, JOM 70 (2018) 1686–1691.

[14] R. Molaei, A. Fatemi, N. Sanaei, J. Pegues, N. Shamsaei, S. Shao, P. Li, D.H. Warner, N. Phan, Fatigue of additive manufactured Ti-6Al-4V, part II: the relationship between microstructure, material cyclic properties, and component performance, Int. J. Fatigue 132 (2020), 105363.

[15] A. Yadollahi, N. Shamsaei, Additive manufacturing of fatigue resistant materials: challenges and opportunities, Int. J. Fatigue 98 (2017) 14–31.

[16] R. Shrestha, J. Simsiriwong, N. Shamsaei, Fatigue behavior of additive manufactured 316L stainless steel parts: Effects of layer orientation and surface roughness, Addit. Manuf. 28 (2019) 23.

[17] A.B. Spierings, N. Herres, G. Levy, Influence of the particle size distribution on surface quality and mechanical properties in AM steel parts, Rapid Prototyp. J. 17 (2011) 195–202.

[18] G. Jacob, C.U. Brown, A. Donmez, The influence of spreading metal powders with different particle size distributions on the powder bed density in laser-based powder bed fusion processes, NIST Adv. Manuf. Ser. 100 (2018).

[19] ASTM B243-20. Standard terminology of powder metallurgy, ASTM Int, 2020.

[20] A. Amado, M. Schmid, G. Levy, K. Wegener, Advances in SLS powder characterization, 22nd Annu, Int. Solid Free. Fabr. Symp. - An Addit. Manuf. Conf. (2011) 438–452.

[21] S. Liu, Y.C. Shin, Additive manufacturing of Ti6Al4V alloy: a review, Mater. Des. 164 (2019), 107552.

[22] ASTM F3001-14, Standard specification for additive manufacturing titanium-6 aluminum-4 vanadium ELI (extra low interstitial) with powder bed fusion, ASTM Int. (2021).

[23] ASTM E1409-13, Standard test method for determination of oxygen and nitrogen in titanium and titanium alloys by inert gas fusion, ASTM Int. (2016).

[24] ASTM E1447-09. Standard test method for determination of hydrogen in titanium and titanium alloys by the inert gas fusion thermal conductivity/infrared detection method, ASTM Int, 2016.

[25] ASTM E1941-04. Standard test method for determination of carbon in refractory and reactive metals and their alloys, ASTM Int, 2016.

[26] ASTM E2371-21, Standard test method for analysis of titanium and titanium alloys by direct current plasma and inductively coupled plasma atomic emission spectrometry (Performance-based test methodology), ASTM Int. (2021).

[27] ASTM B822-20. Standard test method for particle size distribution of metal powders and related compounds by light scattering, ASTM Int, 2020.

[28] M. Tang, P.C. Pistorius, J.L. Beuth, Prediction of lack-of-fusion porosity for powder bed fusion, Addit. Manuf. 14 (2017) 39.

[29] ASTM E466-15. Standard practice for conducting force controlled constant amplitude axial fatigue tests of metallic materials, ASTM Int, 2021.

[30] ASTM E8M-16. Standard test methods for tension testing of metallic materials, ASTM Int, 2016.

[31] M. Frkan, R. Konecna, G. Nicoletto, L. Kunz, Microstructure and fatigue performance of SLM-fabricated Ti6Al4V alloy after different stress-relief heat treatments, Transp. Res. Procedia 40 (2019) 24–29.

[32] ASTM B215-20. Standard practices for sampling metal powders, ASTM Int, 2020.

[33] ASTM B527-15. Standard test method for tap density of metal powders and compounds, ASTM Int, 2020.

[34] ASTM D7891-15. Standard test method for shear testing of powders using the Freeman Technology FT4 powder rheometer shear cell, ASTM Int, 2016.

[35] P. Moghimian, T. Poirié, M. Habibnejad-Korayem, J.A. Zavala, J. Kroeger, F. Marion, F. Larouche, Metal powders in additive manufacturing: A review on reusability and recyclability of common titanium, nickel and aluminum alloys, Addit. Manuf. 102017 (2021).

[36] J.A. Slotwinski, E.J. Garboczi, P.E. Stutzman, C.F. Ferraris, S.S. Watson, M.A. Peltz, Characterization of metal powders used for additive manufacturing, J. Res. Natl. Inst. Stand. Technol. 119 (2014) 460–493.

[37] X. Zhou, N. Dai, X. Cheng, A. Thompson, R. Leach, Three-dimensional characterization of powder particles using X-ray computed tomography, Addit. Manuf. 40 (2021), 101913.

[38] M. Mehrabi, A. Hassanpour, A. Bayly, An X-ray microtomography study of particle morphology and the packing behaviour of metal powders during filling, compaction and ball indentation processes, Powder Technol. 385 (2021) 250–263.

[39] B. Xie, Y. Fan, S. Zhao, Characterization of Ti6Al4V powders produced by different methods for selective laser melting, Mater. Res. Express 8 (2021), 126526.

[40] Freeman Technology, FT4 Powder Rheometer- Summary of Methodologies, 2008.

[41] H.Y. Sohn, C. Moreland, The effect of particle size distribution on packing density, Can. J. Chem. Eng. 46 (1968) 162–167.

[42] M. Ghadiri, M. Pasha, W. Nan, C. Hare, V. Vivacqua, U. Zafar, S. Nezamabadi, A. Lopez, M. Pasha, S. Nadimi, Cohesive powder flow: trends and challenges in characterisation and analysis, KONA Powder Part. J. 37 (2020) 3–18.

[43] T. Voisin, N.P. Calta, S.A. Khairallah, J.B. Forien, L. Balogh, R.W. Cunningham, A. D. Rollett, Y.M. Wang, Defects-dictated tensile properties of selective laser melted Ti-6Al-4V, Mater. Des. 158 (2018) 113–126.

[44] M. Masoomi, S.M. Thompson, N. Shamsaei, Laser powder bed fusion of Ti-6Al-4V parts: thermal modeling and mechanical implications, Int. J. Mach. Tools Manuf. 118–119 (2017) 73–90.

[45] R. Esmaeilizadeh, U. Ali, A. Keshavarzkermani, Y. Mahmoodkhani, E. Marzbanrad, E. Toyserkani, On the effect spatter particles distribution on the quality of Hastelloy X parts made by laser powder-bed fusion additive manufacturing, J. Manuf. Process. 37 (2019) 11–20.

[46] ASTM F2924-14, Standard specification for additive manufacturing titanium-6 aluminum-4 vanadium with powder bed fusion, ASTM Int. (2014).

[47] D. Barba, C. Alabort, Y.T. Tang, M.J. Viscasillas, R.C. Reed, E. Alabort, On the size and orientation effect in additive manufactured Ti-6Al-4V, Mater. Des. 186 (2020), 108235.

[48] W. Xu, M. Brandt, S. Sun, J. Elambasseril, Q. Liu, K. Latham, K. Xia, M. Qian, Additive manufacturing of strong and ductile Ti–6Al–4V by selective laser melting via in situ martensite decomposition, Acta Mater. 85 (2015) 74–84.

[49] R.I. Stephens, A. Fatemi, R.R. Stephens, H.O. Fuchs, Metal fatigue in engineering, John Wiley & Sons, 2000.

[50] S. Romano, P.D. Nezhadfar, N. Shamsaei, M. Seifi, S. Beretta, High cycle fatigue behavior and life prediction for additively manufactured 17-4 PH stainless steel: effect of sub-surface porosity and surface roughness, Theor. Appl. Fract. Mech. 106 (2020), 102477.

[51] J. Pegues, M. Roach, R. Scott Williamson, N. Shamsaei, Surface roughness effects on the fatigue strength of additively manufactured Ti-6Al-4V, Int. J. Fatigue 116 (2018) 543–552.

[52] Y. Murakami, Metal fatigue: Effects of small defects and nonmetallic inclusions, Academic Press, 2019.

[53] Y. Yang, D. Gu, D. Dai, C. Ma, Laser energy absorption behavior of powder particles using ray tracing method during selective laser melting additive manufacturing of aluminum alloy, Mater. Des. 143 (2018) 12–19.

[54] A. Soltani-Tehrani, R. Shrestha, N. Phan, M. Seifi, N. Shamsaei, Establishing specimen property to part performance relationships for laser beam powder bed fusion additive manufacturing, Int. J. Fatigue 151 (2021), 106384.

[55] K. Maeda, S. Suzuki, K. Ueda, T. Kitashima, S.K. Bhattacharya, R. Sahara, T. Narushima, Experimental and theoretical study of the effect of Si on the oxidative behavior of Ti-6Al-4V alloys, J. Alloy. Compd. 776 (2019) 519–528.

[56] T. Deng, S. Li, Y. Liang, L. Sun, Y. Zhang, Effects of scandium and silicon addition on the microstructure and mechanical properties of Ti-6Al-4V alloy, J. Mater. Res. Technol. 9 (2020) 5676–5688.

[57] G.C. Efe, M. Ipek, C. Bindal, S. Zeytin, Pack siliconizing of Ti6Al4V alloy, 132 (2017).

[58] H. Okamoto, J. Phase, O-Si (oxygen-silicon), Equilibr. Diffus 28 (2007) 309–310.

[59] P. Moore, G. Booth, The welding engineer's guide to fracture and fatigue, Elsevier, 2014.

[60] ASTM E2283-08. Standard practice for extreme value analysis of nonmetallic inclusions in steel and other microstructural features, ASTM Int, 2019.

[61] S. Romano, A. Brandão, J. Gumpinger, M. Gschweitl, S. Beretta, Qualification of AM parts: extreme value statistics applied to tomographic measurements, Mater. Des. 131 (2017) 32–48.

[62] S. Beretta, Y. Murakami, Largest-extreme-value distribution analysis of multiple inclusion types in determining steel cleanliness, Metall. Mater. Trans. B 32 (2001) 517–523.

[63] E.J. Gumbel, Statistics of extremes, Columbia University Press, 1958.

[64] S. Romano, A. Brückner-Foit, A. Brandão, J. Gumpinger, T. Ghidini, S. Beretta, Fatigue properties of AlSi10Mg obtained by additive manufacturing: defect-based modelling and prediction of fatigue strength, Eng. Fract. Mech. 187 (2018) 165–189.

[65] S. Beretta, C. Anderson, Y. Murakami, Extreme value models for the assessment of steels containing multiple types of inclusion, Acta Mater. 54 (2006) 2277–2289.